Available online at www.sciencedirect.com

jmr&t Journal of Materials Research and Technology

journal homepage: www.elsevier.com/locate/jmrt

Original Article

Surface layer hardening of metastable austenitic steel – Comparison of shot peening and cryogenic turning

Hendrik Hotz [a,*], *Benjamin Kirsch* [a], *Tong Zhu* [b], *Marek Smaga* [b], *Tilmann Beck* [b], *Jan C. Aurich* [a]

[a] *Technische Universität Kaiserslautern, Institute for Manufacturing Technology and Production Systems, 67653, Kaiserslautern, Germany*

[b] *Technische Universität Kaiserslautern, Institute of Materials Science and Engineering, 67663, Kaiserslautern, Germany*

ARTICLE INFO

Article history:
Received 2 September 2020
Accepted 30 November 2020
Available online 5 December 2020

Keywords:
Surface layer hardening
Metastable austenitic steel
Phase transformation
Shot peening
Cryogenic turning

ABSTRACT

In this paper, the effect of shot peening and cryogenic turning on the surface morphology of the metastable austenitic stainless steel AISI 347 was investigated. In the shot peening process, the coverage and the Almen intensity, which is related to the kinetic energy of the beads, were varied. During cryogenic turning, the feed rate and the cutting edge radius were varied. The manufactured workpieces were characterized by X-ray diffraction regarding the phase fractions, the residual stresses and the full width at half maximum. The microhardness in the hardened surface layer was measured to compare the hardening effect of the processes. Furthermore, the surface topography was also characterized. The novelty of the research is the direct comparison of the two methods with identical workpieces (same batch) and identical analytics. It was found that shot peening generally leads to a more pronounced surface layer hardening, while cryogenic turning allows the hardening to be realized in a shorter process chain and also leads to a better surface topography. For both hardening processes it was demonstrated how the surface morphology can be modified by adjusting the process parameter.

1. Introduction

The properties of component surfaces determine the application behavior to a large extent [1]. In most applications, a low surface roughness and also good mechanical subsurface properties are highly desirable. This includes compressive residual stresses as well as a high microhardness [2].

Metastable austenitic stainless Cr–Ni-steels are widely used in the chemical and petrochemical industries, in power plants, as well as in the food industry, automotive industry and medical technology and are therefore of great economic

* *Corresponding author.*
E-mail address: hendrik.hotz@mv.uni-kl.de (H. Hotz).
URL: https://www.fbk-kl.de

https://doi.org/10.1016/j.jmrt.2020.11.109

importance [3,4]. This group of steels can be hardened by strain hardening mechanisms like twin formation, grain refinement and an increase in the dislocation density [5,6] as well as by martensitic phase transformation from γ-austenite to ε- and α′-martensite (see Fig. 1) [7,8]. It is possible to superimpose these hardening mechanisms in order to further increase the microhardness as well as the tensile and yield strength significantly [9,10]. However, α′-martensite at the component surface can also cause deteriorations of the corrosion resistance [11]. Furthermore, the phase transformation goes along with a decrease in ductility. These disadvantages must be considered when choosing a suitable hardening process depending on the technical application of the component.

The martensitic phase transformation takes place when a minimum difference of free energy is provided [12]. This can be achieved by reducing the temperature below the martensite start temperature M_s. This case is referred to as thermally induced phase transformation. However, for the vast number of austenitic stainless steels the M_s-temperature is in the range of low or even cryogenic temperatures. When superimposed with an external mechanical load, an additional amount of energy difference is provided and the phase transformation already takes place at a higher temperature, e.g. at room temperature (RT).

In the case of a purely elastic deformation this is referred to as stress-induced phase transformation and in the case of a plastic deformation as deformation-induced phase transformation [14]. In addition to the mechanical and thermal load, the austenite stability of a metastable austenitic steel is also dependent on material-specific properties such as the chemical composition and the resulting stacking fault energy [15–17] as well as the grain size. Generally, an increasing amount of alloying elements leads to a higher austenite stability [18]. Most researchers [16,19–21] report, that a decrease in austenite grain size leads to an increase in austenite stability. However, there are also publications showing an inverse effect for ultrafine grains (0.5 μm) [22] and for high grain sizes (52–285 μm) [23]. Besides the impact on the deformation-induced phase transformation, a decrease in the grain size leads to an increase in yield strength and microhardness due to strain hardening according to the Hall-Petch law [24,25].

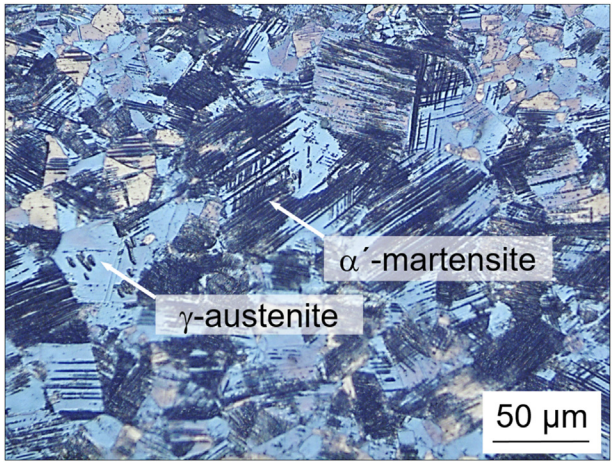

Fig. 1 – Deformation induced ferromagnetic α′-martensite embedded in paramagnetic γ-austenitic matrix after dynamic hardness (Poldi) test in metastable austenitic stainless steels AISI 348 at room temperature, according to [13].

In order to evaluate a materials susceptibility to deformation-induced phase transformation, the M_{d30}-temperature is generally used, at which 50 vol.-% α′-martensite is present after 30% of plastic deformation [26], which is based only on the chemical composition of the material. To determine the susceptibility of the formation of deformation induced α′-martensite in austenitic stainless steels including both (i) the chemical composition as well as (ii) the initial microstructure state, a method based on dynamically applied local plastic deformation and micro-magnetic measurements, was proposed in [13].

There are several mechanical hardening processes for the post-processing of metastable austenitic stainless steels which exploit strain hardening and deformation-induced phase transformation in order to increase the microhardness of the workpiece surface layer. Commonly used mechanical hardening processes are deep rolling [27], machine hammer peening [28] and shot peening [29]. The latter has become widely used in industry. These mechanical hardening processes are usually accompanied with the generation of beneficial compressive residual stresses in the surface layer [2,30].

In shot peening, more pronounced compressive residual stresses can be realized by a higher shot velocity [31]. As the measurement of the shot velocity is difficult and expensive, the Almen intensity is used to characterize the peening process. The Almen intensity, named after John Almen, can be determined with a test strip with a defined geometry and material specifications [32]. The Almen test strip is fixed in a mounting block. After shot peening with a predefined coverage, the Almen test strip arches due to residual stresses. By measuring the arc height of the peened test strip, the Almen Intensity can be determined. The Almen intensity depends on the shot velocity and the weight of the beads [31,32]. With sufficiently low austenite stability, deformation-induced α′-martensite formation can be achieved at RT by shot peening in the workpiece surface layer [33]. Shot peening at cryogenic temperatures leads to a higher amount of deformation-induced α′-martensite, because a part of the required difference in free energy is provided via the temperature reduction [34]. The impact of the beads also leads to a significant grain refinement in the surface layer [35]. The resulting strain hardening in superposition with the deformation-induced formation of α′-martensite leads to an increase in microhardness [36,37]. The beneficial surface layer properties of shot peened austenitic stainless steels cause improvements in the fatigue behavior [38] and the wear resistance [39].

Another method for the hardening of metastable austenitic steels is cryogenic turning [40]. In contrast to mechanical post-treatment processes like shot peening, cryogenic turning integrates the surface layer hardening into the cutting process [41]. This shortens the process chain and thus saves time and resources. Due to the low temperatures and high mechanical loads, cryogenic turning also leads to strain hardening and

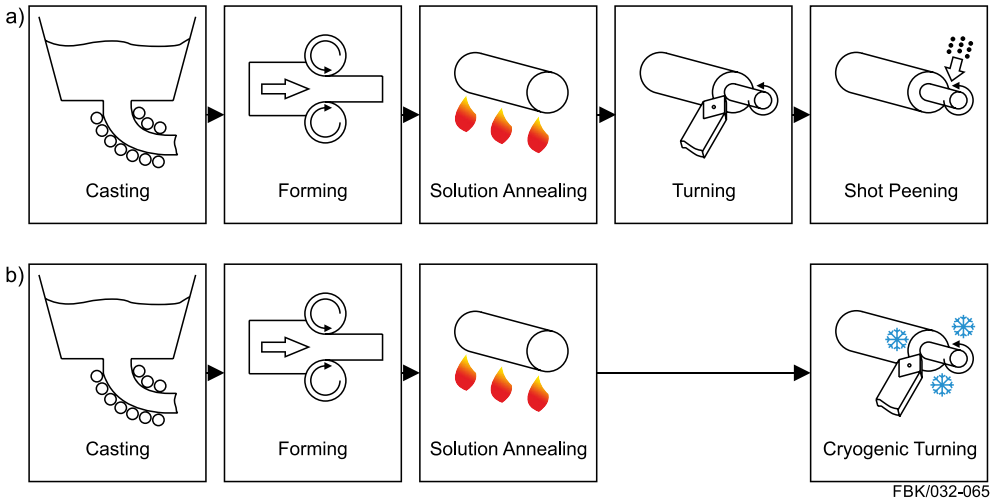

Fig. 2 – Process chains for the manufacture of components with hardened surface layer from metastable austenitic steels: a) conventional process chain, b) surface layer hardening during cryogenic turning, according to [48].

deformation-induced α′-martensite formation in the workpiece surface layer [42]. These beneficial alternations, therefore, result in an increased microhardness [41], higher fatigue strength in High Cycle Fatigue (HCF) regime [43] and in Very High Cycle Fatigue (VHCF) regime [44], as well as an increase in wear resistance [45]. When cryogenically turning different batches, which naturally exhibit varying austenite stability, different contents of α′-martensite occur despite very similar thermomechanical loads [46].

Due to the severe impact of the austenite stability on the metallurgical and mechanical subsurface properties, it is difficult to compare different mechanical hardening processes based on the literature, as each researcher examines a different batch of metastable austenitic steel with different austenite stability. Therefore, the aim of this investigation is to compare the surface layer alternations caused by a cryogenic turning process with those of a shot peening process, when processing the same batch.

The specimens from metastable austenitic stainless steel AISI 347 were manufactured in a conventional process chain where the surface layer hardening is realized by shot peening (see Fig. 2a) and hardened in a cryogenic turning process (see Fig. 2b). In both process chains two significant parameters were varied in the hardening process in order to modify the resulting topography and subsurface properties. When shot peening, the Almen intensity and the coverage were varied. In the cryogenic turning process, modifications were carried out with an adjustment of the feed rate and the cutting edge radius. Measurement data of the cryogenically turned workpieces regarding the magnetic characterization of the martensite content, the microhardness and the average maximum profile height were cited from [47].

The investigations presented in this paper were carried out on the same batch. Therefore, it is possible to compare these two different process chains for the manufacture of austenitic stainless steel components with a hardened surface layer for the first time. The analysis covers the investigation of the resulting deformation-induced martensite formation, microhardness, residual stresses and full width at half maximum as well as a comprehensive investigation of the surface topography and a critical appraisal of the processes.

2. Experimental setup

2.1. *Shot peening*

Ceramic beads with a diameter of 0.4 and 0.6 mm were used for shot peening. The Almen intensity A was measured with a Almen test strip and amounted to $i_1 = 4.5$ A for the small beads and $i_2 = 12.5$ A for the bigger beads. Two different coverages were applied: at a coverage of $c_1 = 100\%$ the entire surface was covered with peening impressions. For the coverage of $c_2 = 400\%$, the peening time was four times as long.

2.2. *Cryogenic turning*

In cryogenic turning, a cutting speed of 30 m/min and a depth of cut of 0.2 mm were used. The feed rate was varied in two stages: $f_1 = 0.15$ mm/rev and $f_2 = 0.35$ mm/rev. A biphase CO_2-solid–gas–mixture was supplied as cooling medium via two external nozzles. Uncoated inserts with the specification DNMA150416 with two different cutting edge radii $r_{\beta,1} = 4$ µm and $r_{\beta,2} = 133$ µm were used. A rake angle of −6° and a tool cutting edge inclination of −7° was used.

2.3. *Measurement technology*

The microstructural characterization of the research material in initial state was done using the electron backscattered diffraction (EBSD) technique. The cross section for EBSD analyse was metallographic prepared and additionally electrolytic polished at 31 V for 20 s using electrolytic polishing and etching device Lectropol-5 (Struers™) with electrolyte A2 (Struers™). The EBSD-measurement was carried out on a scanning electron microscope Quanta 600 FEG (FEI™) with a beam voltage of 20 kV and working distance of 15 mm. The

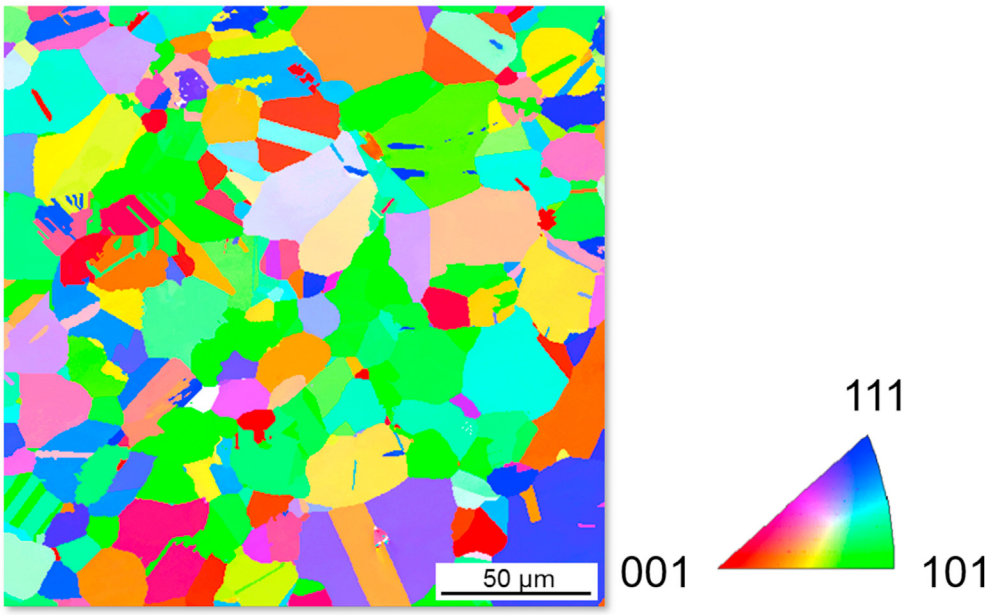

Fig. 3 – EBSD-micrograph of AISI 347 in solution-annealed state.

sample was scanned with a step size of 0.4 µm and the scanning window was 350 × 350 µm.

The surface topography was evaluated via two different methods. To visualize the surfaces, confocal microscopy ([1]Nanofocus™) was used. Extracted 3D-images of a defined area (lateral size: 800 × 800 µm^2) qualitatively showed the effects of the shot peening and turning processes and the varied process parameters on the surface topography. Quantitative roughness measurements were carried out using a tactile measuring device ([1]Mahr™). Total sampling length per roughness profile amounted to 5.6 µm, including a pre- and post-travel length of 0.8 mm each. Each workpiece was measured five times at different radial positions.

For the non-destructive detection of ferromagnetic α′-martensite magnetic [1]Feritscope™ meausrement was performed. When the sensor is placed on the workpiece surface, a current-carrying coil within the measuring probe generated a magnetic field whose field lines flowed through the workpiece subsurface to a depth of approx. 3.5 mm. The magnetic field interacted with the ferromagnetic phase fractions (here: α′-martensite) and induced a voltage in a second coil, which represented the measuring signal and could be converted linearly into the ferromagnetic phase component. The α′-martensite content was determined by multiplying the measurement signal (FE-%) by a factor of 1.7, according to [49]. As the martensite content in the subsurface can vary depending on the location [50], the workpieces were each examined with a grid of five measuring points in the longitudinal direction and eight measuring points in the circumferential direction in order to determine a representative mean value. However, with the magentic method it is not possible to detect the paramagnetic ε-martensite or to determine the phase distribution.

The distribution of phase fraction (γ-austenite, α′-martensite and ε-martensite) and residual stress states were aquired via systematic combination of X-ray diffraction (XRD) measurements and electrolytic removals using electrolyte A2 (Struer™), the removed layer depth was measured with a high-resolusion indicator (Kaefer™) after each removal process. The XRD data was recorded on a laboratory diffractometer ([1]Malvern Panalytical™) with Cu-$K_{\alpha 1}$ radiation at 40 kV and 40 mA. A spot size of 1.5 × 1.5 mm was used for both analysis methods. For the phase fraction determination, the data was collected over the range 40° < 2θ < 100° with a scanning speed of 0.005°/s. The experimental data was evaluated using the XRD-analysis software HighScore Plus ([1]Malvern Panalytical™) for the quantitative phase analysis and line profile analysis by means of Rietveld-refinement method and pseudo-Voigt profile function. For the determination of macro residual stresses, the samples were investigated using $\sin^2\psi$ method with 8 different ψ angles from − 69.30 to +69.30° on the diffraction peak of the (022) austenite lattice plane. The scanning parameters were defined with a finer range of 72.72° < 2θ < 76.68° and lower scanning speed at 0.003°/s. The scanned data was fitted using the modified Lorentzian function in the software X'Pert Stress ([1]Malvern Panalytical™), elastic constants of austenitic stainless steels are referred to [51].

In order to determine the microhardness in the subsurface after the hardening processes, measurements were carried out on cross sections of the workpieces with a vickers indenter with a load force of 98.1 mN (HV 0.01) and a loading time of 10 s. Indentations were made in a range from 20 to 400 µm below the surface at 10 µm intervals for the development of microhardness profiles. Three measurement points per distance were performed for statistical verification.

[1] Naming of specific manufacturers is done solely for the sake of completeness and does not necessarily imply an endorsement of the named companies nor that the products are necessarily the best for the purpose.

Table 1 – Chemical composition of AISI 347 in weight-%.

C	N	Cr	Ni	Mo	Nb	Cu	Mn	Si	P	Cu	Fe
0.02	0.02	17.19	9.44	0.23	0.38	0.11	1.55	0.02	0.02	0.11	balance

2.4. *Workpiece material*

The investigated material was the metastable austenitic stainless steel AISI 347 (X6CrNiNb1810, 1.4550), manufactured by Deutsche Edelstahlwerke GmbH, delivered as rolled bars with a diameter of 25 mm, in solution annealed state from one single batch. To obtain a fully austenitic microstructure, an additional solution annealing at 1050 °C for 35 min followed by quenching in helium atmosphere was performed in an industrial heat treatment furnace. Grain orientation maps determined by EBSD at initial state is shown in Fig. 3, which shows a homogeneous pure austenitic microstructure with annealing twins in different sizes. Without consideration of twin boundaries, the equivalent grain diameters were estimated as 18 μm. No preferred orientation can be observed in solution-annealed state.

The chemical composition of the investigated AISI 347 steel is given in Table 1. The mechanical properties and the characteristic parameters of metastabilty, i.e. M_s- and M_{d30}-temperatures calculated according to the empirical equations given by Eichelmann [12] and Angel [26], respectively of investigated material are given in Table 2.

2.5. *Workpiece preparation and initial surface layer properties*

The rod material was turned with a cutting speed of 100 m/min, a depth of cut of 0.4 mm and a feed rate of 0.1 mm/rev to a diameter of 14.4 mm. A conventional emulsion was supplied as flood cooling lubrication. Coated carbide inserts with chip breaker were used.

The workpieces had periodical roughness peaks characteristic for the turning process and an average maximal profile height R_z of 4.28 ± 0.93 μm. The measurements with the magnetic sensor revealed an average α′-martensite content of 0.46 ± 0.13 vol.-% after workpiece preparation. This shows, that even during this conventional turning process, deformation-induced phase transformation occurred in the workpiece subsurface to a minor extent. A microhardness of 289 ± 8 HV0.01 was measured at a distance of 20 μm form to the surface, which was already significantly higher than the core microhardness HV_0 = 196 ± 6 HV0.01.

In the conventional process chain, the workpieces prepared in this way with a diameter of 14.4 mm were hardened with shot peening. In the process chain, in which surface layer hardening is achieved by the cryogenic turning process, the workpieces are turned from 14.4 mm to a final diameter of 14 mm via cryogenic turning.

Table 2 – Mechanical properties and characteristic parameters of metastability.

$R_{p0.2}$ in MPa	UTS in MPa	M_{d30} in °C	M_S in °C
225	603	46	−87

3. Surface topography

Shot peening and cryogenic turning led to distinctly different surface topographies. In shot peening the impulse of the beads created craters on the surface (see Fig. 4a-d). During cryogenic turning, the surface is decisively governed by the process kinematics and the tool macro geometry, which led to periodical roughness peaks (see Fig. 4e-h).

When increasing the intensity during shot peening, the diameter and the depth of the craters increased, as well as the height of the adjacent material build-ups which led to a higher average maximum profile height R_z (see Fig. 5a). The fourfold increase of the coverage caused a flattening of the roughness peaks and thus less pronounced craters on the surface. This resulted in a minor decrease of the surface roughness for i_2, and no significant changes for i_1, where both c_1 and c_2 led to rather low roughness values.

Increasing the feed rate during cryogenic turning resulted in an increased height of the periodical roughness peaks as well as an increased distance between them due to the changed workpiece trajectory. As it is well known from literature [52], the theoretical kinematic surface roughness increases squarely with the feed rate. However, with rising cutting edge radius ploughing effects were promoted, which led to increased material build-up on the roughness peaks and thus resulted in an increased average maximum profile height R_z (see Fig. 5b). Overall, cryogenic turning led to a lower surface roughness than shot peening.

4. Subsurface properties

4.1. *Magnetic characterization*

After shot peening as well as after cryogenic turning, a significant increase in α′-martensite was detected in the workpiece subsurfaces (see Fig. 6), compared to the initial state after workpiece preparation (0.46 ± 0.13 vol.-% α′-martensite). The deformation-induced α′-martensite formation during shot peening was caused by the high mechanical load at RT. During cryogenic turning, besides the high mechanical load due to high passive forces (approx. 150–325 N [47]), also lowered temperatures in the subsurface (approx. 250–270 K [53]) contributed to the difference in free energy required for phase transformation. In both hardening processes, a variation of the process parameters led to a difference in the resulting α′-martensite content.

In shot peening, an increase in coverage from 100% to 400% caused a significant increase in the α′-martensite content (450% at i_1 and 213% at i_2). This can be explained by the fact

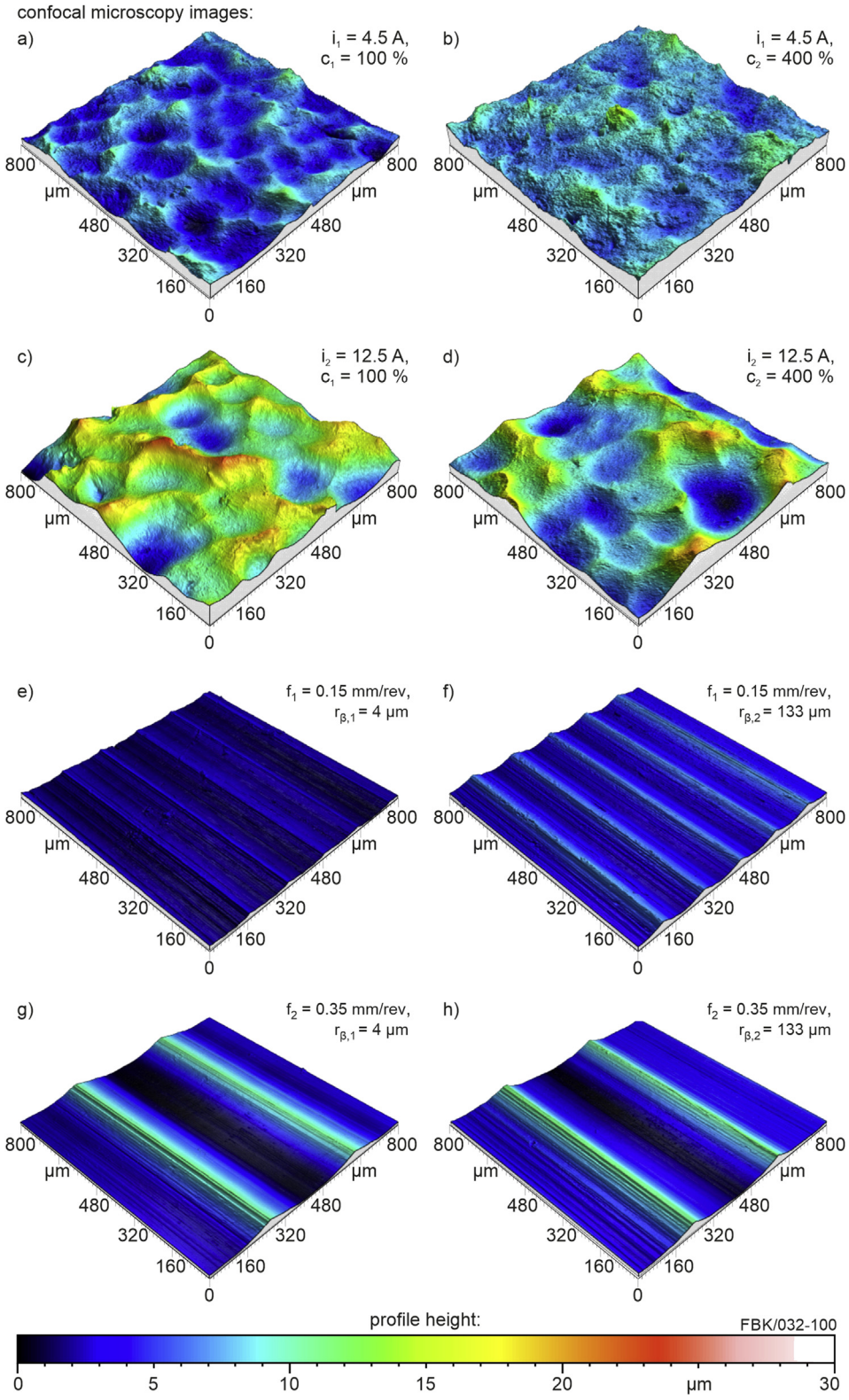

Fig. 4 – Surface topography after a-d) shot peening; e-h) cryogenic turning.

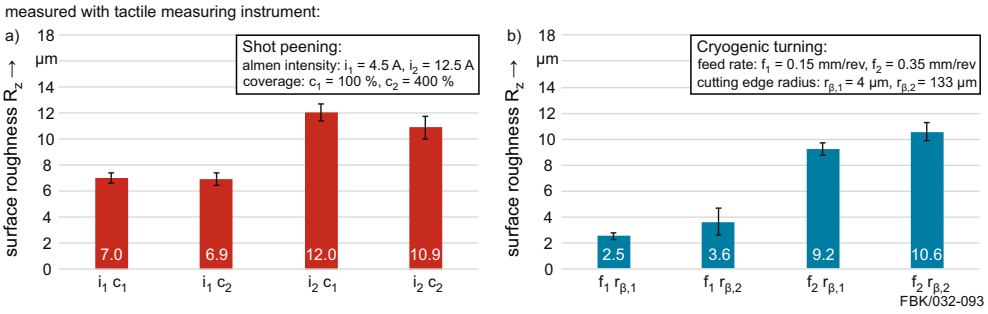

Fig. 5 – Average maximum profile height R_z after a) shot peening; b) cryogenic turning.

that more beads hit the surface with an increase in blasting time and the subsurface was deformed more severely, which favored the deformation-induced phase transformation. An increase in intensity, i.e. a higher kinetic energy of the beads, led to an increase in the α′-martensite content of 77% at low coverage c_1. At high coverage c_2 no significant increase can be observed. However, the standard deviations for the measured martensite content were fairly high at c_2. As the martensite content could not be increased despite higher kinetic energy and the associated higher deformation in the subsurface, this could already imply saturation.

During cryogenic turning, an increase in the cutting edge radius led to an increase in the passive forces without significantly impacting the temperatures [41]. The higher mechanical loads at comparable temperatures represent a more favorable thermomechanical load for the deformation-induced phase transformation. Thus, higher α′-martensite contents could be determined at both feed rates with increasing cutting edge radius (91% increase at f_1 and 66% increase at f_2). An increase in the feed rate led to a larger cross section of undeformed chip and thus to higher passive forces. However, the increase in the feed rate also resulted in a shorter cutting time. Thus, the workpiece was cooled less by the cryogenic cooling medium, so that the temperatures in the subsurface at f_2 were about 20 K higher than at f_1 [53]. However, the influence of the higher mechanical load outweighed the higher temperatures counteracting the phase transformation, since higher α′-martensite contents were measured at both cutting edge radii with increasing feed rates (61% increase at $r_{β,1}$ and 40% increase at $r_{β,2}$).

4.2. *X-ray characterization*

Fig. 7 shows the results of quantitative X-ray phase fraction analysis. In comparison with the magnetic characterization (see Fig. 6), X-ray analysis reveals more details about the distribution of α′-martensite and allows the estimation of the fraction of paramagnetic ε-martensite as well. The maximum phase fraction of ε-martensite was always below 20 vol.-% and mostly occurred in greater depth from the surface.

Among the different parameters of the shot peening process, the coverage plays the most significant role on the depth profile of the phase fraction. Both 100% covered workpieces showed a maximum volume fraction of deformation induced α′-martensite (37.6 vol.-% of i_1 and 11.9 vol.-% of i_2) directly on the workpiece surface and decreased continuously in the subsurface. As the coverage increased from 100 to 400%, the volume fraction of α′-martensite as well as transformation depth was heavily increased. The maximum values of α′-martensite volume fraction were found in the subsurface within 50 µm from the surface, which might be explained by the maximum Hertzian stress, which presumably is not located directly at the surface but within the workpiece subsurface [54]. An increase in Almen intensity led to higher transformation depths (see Fig. 7a, b) but lower maximum values of martensite volume fraction (see Fig. 7a) in the subsurface. This might be traced back to the fact that beads with

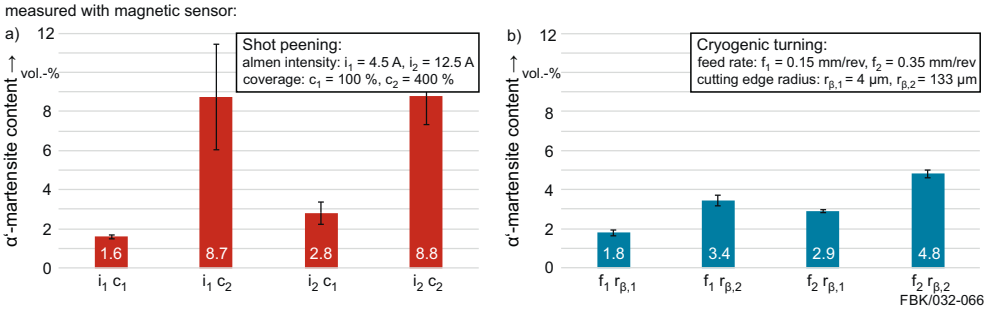

Fig. 6 – Martensite content in the workpiece subsurface after a) shot peening; b) cryogenic turning.

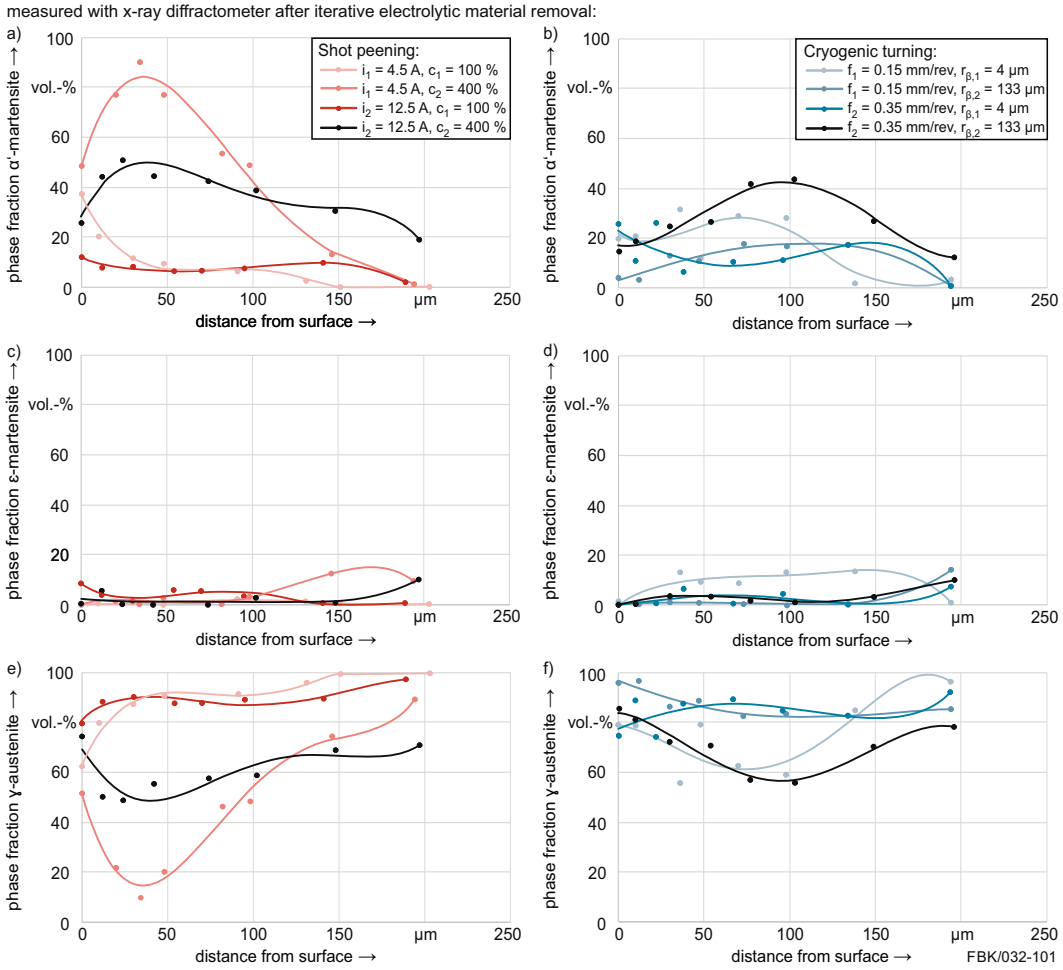

Fig. 7 – Phase fractions in the workpiece subsurface after a, c, e) shot peening; b, d, f) cryogenic turning.

greater diameter cause a shift in the Hertzian stress distribution, leading to a less pronounced maximum value which is located in greater distance from the surface.

Similar influences from the shot peening parameters can be observed on the ε-martensitic transformation process according to Fig. 7c. Increasing coverage led to a clearly deepening of the transformation start position as well as the transformation depth. Compared to both 100% covered workpieces, ε-martensite can be firstly detected in the depths of around 100 or 150 µm on the 400% covered workpieces. Since the phase fraction of ε-martensite was relatively low in the tested range, it is less possible to determine the influences from the changing parameters explicitly.

In the cryogenic turning process, the workpiece manufactured with higher feed rate and larger cutting edge radius showed a predominant transformation behavior and the

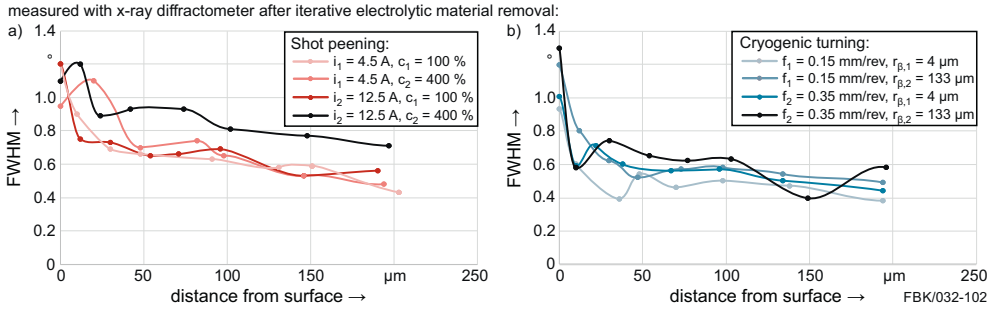

Fig. 8 – FWHM in the workpiece subsurface after a) shot peening; b) cryogenic turning.

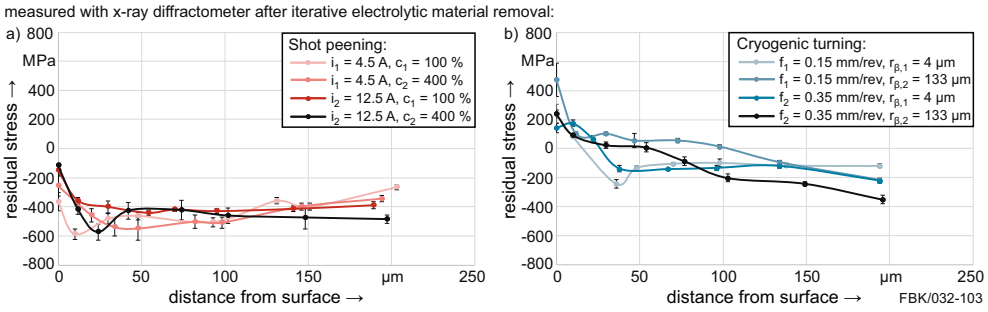

Fig. 9 – Residual stresses in the workpiece subsurface after a) shot peening; b) cryogenic turning.

maximum volume fraction of α'-martensite has reached 43 vol.-% at around 100 µm from the surface. Turned at lower feed rate and smaller cutting edge radius, the workpiece showed a transformation depth of around 180 µm according to Fig. 7f. An increase in cutting edge radius, in terms of higher passive force, could clearly extend the transformation depth. It should be noted that the changing parameters could additionally influence the position of maximum α'-martensite volume fraction, which could possibly be explained by the complex thermomechanical loadings during the cryogenic turning process. The high friction caused by turning led to rash temperature increase near the workpiece surface. Moreover, the high strain rate in the near-surface regime can also suppress the $\gamma \rightarrow \alpha'$ transformation due to adiabatic heating of the substrate material [49]. These thermal influences sometimes lead to a more convenient phase transformation conditions in the subsurface region instead of direct on the workpiece surface.

No ε-martensitic transformation directly at the surface could be detected for all cryogenically turned workpieces. In the subsurface, the minimum loaded workpiece showed the highest volume fraction of ε-martensite with an almost constant value of around 13% from 36 to 138 µm. Due to the lowest transformation depth, ε-martensitic transformation was again not detectable over 194 µm. With increased mechanical loads during cryogenic turning, less ε-martensite can be seen in the near surface regime; probably because most of the created ε-martensite is directly transformed into α'-martensite. A clear increase of the ε-martensite fraction can be determined at around 150 µm from the surface, where the mechanical loads were not sufficient for a subsequent transformation into α'-martensite.

For further characterization, line profile analysis was done to acquire the full width at half maximum (FWHM) of the (022) austenite peaks in the X-ray spektra, the results were shown in Fig. 8. The increase of FWHM can be correlated with microstrucral changes in the test range: crystal size, microstrain, increase of density of lattice defects e.g. the increase of dislocation density, building up of stacking faults etc. in crystaline materials [55]. Regardless of the processing methods or parameters, a generally declining trend of FWHM value could be determined from the workpiece surface to the subsurface. However, the decrease is much steeper in the near surface regime of the cryogenically turned workpieces.

Influenced by different processing parameters, the FWHM values of shot peened workpieces vary from 0.95 to 1.2° on the surface. Compared to the values from 0.43 to 0.71° in the subsurface, the significant difference can be related to the formation of nanocrystalline layer on the specimen surface, and also increase of lattice defects in the near surface regime caused by plastic deformation. Both 100% covered workpieces showed a strong decrease of the FWHM-value in the first 30 µm from the surface, which then drop off relatively smooth. At a higher coverage of 400%, the FWHM values on the workpiece surface were slightly lower than the 100% covered samples. An increase until the maximum value at around 10–20 µm could be determined (see Fig. 8a). A steep descent in the next 20 µm was observed, followed by gradually decrease.

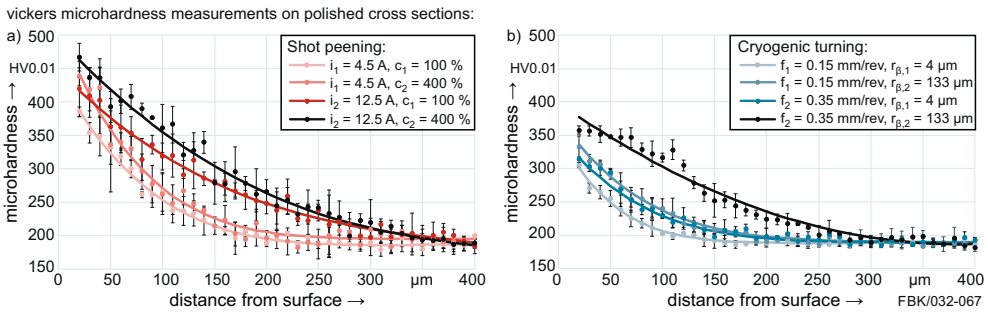

Fig. 10 – Microhardness in the workpiece subsurface after a) shot peening; b) cryogenic turning.

It should be mentioned, that the workpieces processed with the maximum Almen intensity and coverage showed a considerably higher FWHM value compared to the other shot peening parameters.

In Fig. 8b, both workpieces turned with greater cutting edge radius showed higher FWHM-values at the surface, because of the higher mechanical loads and thus pronounced plastic deformation in the near surface regime. With the lower feed rate of $f_1 = 0.15$ mm/rev, the FWHM values dropped heavily in the first 40 μm from the surface and then remained relatively stable. As the feed rate was increased to 0.35 mm/rev, the steep descent of FWHM values could be determined within the first 10 μm. In the next 10–20 μm, the FWHM values rose again to a subpeak and then dropped continuously to the workpiece interior, which indicates a more complicated microstructure evolution process due to the interaction of thermo-mechanical loads.

4.3. *Residual stresses*

Fig. 9 shows the residual stress profiles of workpieces manufactured with both processes and various parameters. Generally, the residual stresses varied greatly between the two processes, but were only slightly impacted by the variation of the process parameters. In all cases, compressive residual stresses were determined in the first 200 μm in the workpieces subsurface after shot peening (see Fig. 9a). These results match well with the literature, since compressive residual stresses are typical for shot peened workpieces [56]. After cryogenic turning, tensile resdual stresses were detected in the near surface regions and converted to compressive residual stress in the subsurface (see Fig. 9b), which is also in good agreement with literature [57].

Compressive residual stresses were induced by the plastic deformation during the shot peening process [56]. "S-shaped" depth profiles of residual stress could be observed in most shot peened workpieces (see Fig. 9a). When increasing the Almen intensity during shot peening, the compressive residual stresses were slightly relieved directly on the workpiece surface. A higher coverage also led to lower compressive residual stresses on the surface. Regarding the course of the residual stress profiles in the subsurface, no clear trend regarding the impact of the Almen intensity or the coverage can be identified. The maximum values were detected within the first 50 μm under the surface (see Fig. 9a).

During the cryogenic turning, tensile residual stresses were induced in the near surface regime due to high thermal loads caused by high friction, meanwhile the deformation in the surface layer led to compressive residual stresses deep in the subsurface. Both workpieces turned with the cutting edge radius of 133 μm showed higher maximum value of tensile residual stresses and a deeper tensile residual stress range. The converting point from tensile residual stress to compressive residual stress lay at around 50 and 100 μm under the workpiece surface for lower feed rate of $f_1 = 0.15$ mm/rev and higher with $f_2 = 0.35$ mm/rev, respectively, while the minor cutting edge radius $r_{ß,1} = 4$ μm performed converting points at only around 20–25 μm under the surface. Besides, the stress influenced depths were also related to the cutting edge radius, which showed a flat plateau over 50 μm on the workpiece turned with the lower cutting edge radius of 4 μm, while the others still showed a falling trend at around 200 μm, which indicates the stress influenced range might be even deeper in the subsurface.

4.4. *Microhardness*

Fig. 10 shows the microhardness profiles of the workpieces of the metastable austenitic steel AISI 347 after shot peening and after cryogenic turning. A significant increase in microhardness was measured for all workpieces, whereby the maximum microhardness was always determined at the measurement position closest to the surface. In both shot peened and cryogenically turned workpieces, the microhardness increase resulted from a superposition of deformation-induced phase transformation and strain hardening. While the process parameters in both processes had a significant influence on the microhardness, the microhardness after shot peening was generally higher.

An increase in coverage, as well as an increase in intesity led to a higher maximum microhardness. A higher intensity also led to a significant increase in the microhardness depth. This can be led back to the fact that the larger beads, when hitting the surface, distributed their load to a greater volume. Furthermore the mechanical load implied by a single bead was also higher due to the increased kinetic energy. The resulting differences in Hertzian stress led to microstructural changes in a greater depth beneath the surface, which ultimately resulted in the higher hardness depth. The high increase in α'-martensite content with increasing coverage (see Figs. 6 and 7a) allows the assumption that the coverage would have a greater influence on the microhardness than the intensity. However, this could not be observed, which leads to the conclusion that a significant proportion of the microhardness increase in the subsurface of the shot peened workpieces was due to strain hardening. This is in agreement with the higher FWHM values measured in the specimen after shot peening with high intensity (see Fig. 8a).

In cryogenic turning, a higher feed rate, as well as a larger cutting edge radius led to an increase in the maximum microhardness and hardness depth. Even when turning with f_1 and $r_{ß,1}$ the microhardness increase was higher compared to the workpieces manufactured with a conventional turning process (see section 2.5), which can be explained by the beneficial effect of the cryogenic cooling on strain hardening and deformation-induced phase transformation. Contrary to the shot peened workpieces, there was a very good correlation between α'-martensite content (see Figs. 6 and 7b) and microhardness (see Fig. 10b) after cryogenic turning. However, the FWHM values were also higher with increasing feed rate and cutting edge radius (see Fig. 8b). Thus, strain hardening might also have significantly impacted the increase in microhardness.

5. Conclusions and outlook

In this paper, the effect of shot peening and cryogenic turning on surface morphology of the metastable austenitic stainless steel AISI 347 was investigated. The surface topography, the extent of phase transformations (deformation induced α'-martensite and ε-martensite formation), the residual stresses, the full width at half maximum and the microhardness in dependence of the Almen intensity and coverage when shot peening as well as in dependence of feed rate and cutting edge radius when cryogenic turning was quantified.

The results can be summarised as follows:

- Both processes result into a significant increase in phase transformations, microhardness and induced compressive stresses. Both processes are hence suitable for surface hardening.
- Comparing the two methods:
  - o Concerning the surface topography, cryogenic turning resulted in a more uniform pattern and lower roughness values
  - o Concerning deformation induced martensite formation, shot peening resulted in a more pronounced phase transformation
  - o Concerning residual stresses, shot peening resulted into stronger compressive stresses, completely avoiding tensile stresses within the near surface regime; while cryogenic turning exhibited low tensile stresses directly near the surface, switching to compressive stresses within approximately 50 μm from the surface.
  - o Concerning microhardness, shot peening achieved overall higher microhardness values.

In conclusion, cryogenic turning can be used as an alternative to the separate process step of shot peening when a less pronounced surface hardening is sufficient for the given application, with the advantage that a more uniform surface topography and a lower surface roughness can be realized, while also shortening the process chain. Future investigations will focus on the correlations between alternation in the surface morphology and resulting fatigue behaviour.

Declaration of Competing Interest

The authors declare that they have no known competing financial interests or personal relationships that could have appeared to influence the work reported in this paper.

Acknowledgements

This work was supported by the Deutsche Forschungsgemeinschaft (DFG, German Research Foundation) - project number 172116086 - SFB 926.

REFERENCES

[1] Jawahir IS, Attia H, Biermann D, Duflou J, Klocke F, Meyer D, et al. Cryogenic manufacturing processes. CIRP Annals 2016;65(2):713–36. https://doi.org/10.1016/j.cirp.2016.06.007.
[2] Jawahir IS, Brinskmeier E, M'Saoubi R, Aspinwall DK, Outeiro JC, Meyer D, et al. Surface integrity in material removal processes: recent advances. CIRP Annals 2011;60(2):603–26. https://doi.org/10.1016/j.cirp.2011.05.002.
[3] Marshall P. Austenitic stainless steels – microstructure and mechanical properties. London, United Kingdom: Elsevier Applied Science; 1984.
[4] Hunscha G, Grundmann R, Stellfeld I, Michel P, Roth P, Paus A, et al. Anwendungen. In: Verein Deutscher Eisenhüttenleute (VDEh) Nichtrostende Stähle. 2nd ed. Düsseldorf, Germany: Verlag Stahleisen GmbH; 1989. p. 243–99.
[5] Lei C, Deng X, Li X, Wang Z, Wang G, Misra RDK. Mechanical properties and strain hardening behavior of phase reversion-induced nano/ultrafine Fe-17Cr-6Ni austenitic structure steel. J Alloys Compd 2016;689:718–25. https://doi.org/10.1016/j.jallcom.2016.08.020.
[6] Yi HY, Yan FK, Tao NR, Lu K. Work hardening behavior of nanotwinned austenitic grains in a metastable Austenitic stainless steel. Scripta Mater 2016;114:133–6. https://doi.org/10.1016/j.scriptamat.2015.12.021.
[7] Olson GB, Cohen M. Kinetics of strain-induced martensitic nucleation. Metall Mater Trans A 1975;6A:791–5. https://doi.org/10.1007/BF02672301.
[8] Hecker SS, Stout MG, Staudhammer KP, Smith JL. Effects of strain state and strain rate on deformation-induced transformation in 304 stainless steel: Part I. Magnetic measurements and mechanical behavior. Metall Mater Trans A 1982;13:619–26. https://doi.org/10.1007/BF02644427.
[9] Meyer D. Cryogenic deep rolling – an energy based approach for enhanced cold surface hardening. CIRP Ann - Manuf Technol 2012;61(1):543–6. https://doi.org/10.1016/j.cirp.2012.03.102.
[10] Smaga M, Skorupski R, Eifler D, Beck T. Microstructural characterization of cyclic deformation behavior of metastable austenitic stainless steel AISI 347 with different surface morphology. J Mater Res 2017;32:4452–60. https://doi.org/10.1557/jmr.2017.318.
[11] Wang B, Hong C, Winther G, Christiansen TL, Somers MAJ. Deformation mechanisms in meta-stable and nitrogen-stabilized austenitic stainless steel during severe surface deformation. Materialia 2020;12:100751. https://doi.org/10.1016/j.mtla.2020.100751.
[12] Eichelmann AH, Hull FC. The effect of composition on the temperature of spontaneous transformation of austenite to martensite in 18-8 type stainless steel. Transactions of the ASM 1953;45:77–104.
[13] Smaga M, Boemke A, Tobias D, Klein M. Metastability and fatigue behavior of austenitic stainless steels. In: MATEC web of conferences; Les Ulis Bd. 165 Les Ulis. EDP Sciences; 2018. https://doi.org/10.1051/matecconf/201816504010.
[14] Olson GB, Cohen M. A mechanism for the strain-induced nucleation of martensitic transformations. J Less Common Met 1972;28(1):107–18. https://doi.org/10.1016/0022-5088(72)90173-7.
[15] Monkman FC, Cuff FB, Grant NJ. Computation of Ms for stainless steels. Metal Progress 1957;71(4):94–6.
[16] Nohara K, Ono Y, Ohashi N. Composition and grain size dependencies of strain-induced martensitic transformation

in metastable Austenitic stainless steels. Tetsu-To-Hagane 1977;63(5):772–82. https://doi.org/10.2355/tetsutohagane1955.63.5_772.
[17] Venables JA. The martensite transformation in stainless steel. Phil Mag: J Theoret Exp Appl Phys 1962;7(73):35–44. https://doi.org/10.1080/14786436208201856.
[18] Soleimani M, Kalhor A, Mirzadeh H. Transformation-induced plasticity (TRIP) in advanced steels: a review. Mater Sci Eng, A 2020;795:140023. https://doi.org/10.1016/j.msea.2020.140023.
[19] Raman SGS, Padmanabhan KA. Influence of martensite formation and grain size on room temperature low cycle fatigue behaviour of AISI 304LN austenitic stainless steel. Mater Sci Technol 1994;10/7:614–20. https://doi.org/10.1179/mst.1994.10.7.614.
[20] Yoo CS, Park YM, Jung YS, Lee YK. Effect of grain size on transformation-induced plasticity in an ultrafine-grained metastable austenitic steel. Scripta Mater 2008;59/1:71–4. https://doi.org/10.1016/j.scriptamat.2008.02.024.
[21] Das A, Tarafder S, Chakraborti PC. Estimation of deformation induced martensite in aus-tenitic stainless steels. Mater Sci Eng A 2011;529:9–20. https://doi.org/10.1016/j.msea.2011.08.039.
[22] Kisko A, Misra RDK, Talonen J, Karjalainen LP. The influence of grain size on the strain-induced martensite formation in tensile straining of an austenitic 15Cr–9Mn–Ni–Cu stainless steel. Mater Sci Eng A 2013;579:408–16. https://doi.org/10.1016/j.msea.2013.04.107.
[23] Shrinivas V, Varma SK, Murr LE. Deformation-induced martensitic characteristics in 304 and 316 stainless steels during room-temperature rolling. Metall Mater Trans A 1995;26:551–671. https://doi.org/10.1007/BF02663916.
[24] Nasiri Z, Ghaemifar S, Naghizadeh M, Mirzadeh H. Thermal mechanisms of grain refinement in steels: a review. Met Mater Int 2020. https://doi.org/10.1007/s12540-020-00700-1.
[25] Naghizadeh M, Mirzadeh H. Processing of fine grained AISI 304L austenitic stainless steel by cold rolling and high-temperature short-term annealing. Mater Res Express 2018;5:5. https://doi.org/10.1088/2053-1591/aac461.
[26] Angel T. formation of martensite in austenitic stainless steels. Effect of deformation, temperature, and composition. J Iron Steel Inst 1954;177:165–74.
[27] Brinksmeyer E, Garbrecht M, Meyer D. Cold surface hardening. CIRP Ann - Manuf Technol 2008;57:541–4. https://doi.org/10.1016/j.cirp.2008.03.100.
[28] Schulze V, Bleicher F, Groche P, Guo YB, Pyun YS. Surface modification by machine hammer peening and burnishing. CIRP Ann - Manuf Technol 2016;65(2):809–32. https://doi.org/10.1016/j.cirp.2016.05.005.
[29] Horowitz I. Oberflächenbehandlung mittels Strahlmitteln – Handbuch über Strahltechnik und Strahlanlagen – Band 1: Die Grundlagen der Strahltechnik. Essen, Germany: Vulkan-Verlag; 1982.
[30] Gallitelli D, Boyer V, Gelineau M, Colaitis Y, Rouhaud E, Retraint D, et al. Simulation of shot peening: from process paramaters to residual stress fields in a structure. Compt Rendus Mec 2016;344(4–5):355–74. https://doi.org/10.1016/j.crme.2016.02.006.
[31] Cao W, Fathallah R, Castex L. Correlation of almen arc height with residual stresses in shot peening process. Mater Sci Technol 1995;11(9):967–73. https://doi.org/10.1179/mst.1995.11.9.967.
[32] Champaigne J. Shot peening intensity measurement, vol. 6. The Shot Peener; 1992. p. 1–6.
[33] Guiheux R, Berveiller S, Kubler R, Bouscaud D, Patoor E, Puydt Q. Martensitic transformation induced by single shot peening in a metastable Austenitic stainless steel 301LN: experiments and numerical simulation. J Mater Proces 2017;249:339–49. https://doi.org/10.1016/j.jmatprotec.2017.06.015.
[34] Novelli M, Fundenberger J-J, Bocher P, Grosdidier T. On the effectiveness of surface severe plastic deformation by shot peening at cryogenic temperature. Appl Surf Sci 2016;389:1169–74. https://doi.org/10.1016/j.apsusc.2016.08.009.
[35] Unal O, Varol R. Surface severe plastic deformation of AISI 304 via conventional shot peening, severe shot peening and repeening. Appl Surf Sci 2015;351:289–95. https://doi.org/10.1016/j.apsusc.2015.05.093.
[36] Bagherifard S, Slawik S, Fernández-Pariente I, Pauly C, Mücklich F, Guagliano M. Nanoscale surface modification of AISI 316L stainless steel by severe shot peening. Mater Des 2016;102:68–77. https://doi.org/10.1016/j.matdes.2016.03.162.
[37] Fargas GR, Roa JJ, Mateo A. Effect of shot peening on metastable Austenitic stainless steels. Mater Sci Eng 2015;641:290–6. https://doi.org/10.1016/j.msea.2015.05.079.
[38] Azar V, Hashemi B, Yazdi MR. The effect of shot peening on fatigue and corrosion behavior of 316L stainless steel in Ringer's solution. Surf Coating Technol 2010;204:3546–51. https://doi.org/10.1016/j.surfcoat.2010.04.015.
[39] AlMangour B, Yang J-M. Improving the surface quality and mechanical properties by shot-peening of 17-4 stainless steel fabricated by additive manufacturing. Mater Des 2016;110:914–24. https://doi.org/10.1016/j.matdes.2016.08.037.
[40] Aurich JC, Mayer P, Kirsch B, Eifler D, Smaga M, Skorupski R. Characterization of deformation induced surface hardening during cryogenic turning of AISI 347. CIRP Annals 2014;63/1:65–8. https://doi.org/10.1016/j.cirp.2014.03.079.
[41] Hotz H, Kirsch B. Influence of tool properties on thermomechanical load and surface morphology when cryogenically turning metastable Austenitic steel AISI 347. J Manuf Process 2020;52:120–31. https://doi.org/10.1016/j.jmapro.2020.01.043.
[42] Hotz H, Kirsch B, Aurich JC. Impact of the thermomechanical load on subsurface phase transformations during cryogenic turning of metastable austenitic steels. J Intell Manuf 2020. https://doi.org/10.1007/s10845-020-01626-6.
[43] Smaga M, Hahnenberger F, Sorich A, Eifler D. Cyclic deformation behavior of austenitic steels in the temperature range -60°C ≤T ≤550°C. Key Eng Mater 2011;465:439–42. https://doi.org/10.4028/www.scientific.net/KEM.465.439.
[44] Smaga M, Boemke A, Daniel T, Skorupski R, Sorich A, Beck T. Fatigue behavior of metastable Austenitic stainless steels in LCF, HCF and VHCF regimes at ambient and elevated temperatures. Metals 2019;9(6):704. https://doi.org/10.3390/met9060704.
[45] Frölich D, Magyar B, Sauer B, Mayer P, Kirsch B, Aurich JC, et al. Investigation of wear resistance of dry and cryogenic turned metastable austenitic steel shafts and dry turned and ground carburized steel shafts in the radial shaft seal ring system. Wear 2015;328–329:123–31. https://doi.org/10.1016/j.wear.2015.02.004.
[46] Kirsch B, Hotz H, Müller R, Becker S, Boemke A, Smaga M, et al. Generation of deformation-induced martensite when cryogenic turning various batches of the metastable Austenitic steel AISI 347. J Inst Eng Prod 2019;13:343–50. https://doi.org/10.1007/s11740-018-00873-0.
[47] Hotz H, Kirsch B, Gutwein S, Becker S, von Harbou E, Müller R, et al. Kryogenes Drehen von X6CrNiNb18-10 - Einfluss des Schneidkantenradius auf Prozesskräfte und Prozessergebnisgrößen. wt Werkstattstechnik online 2018;108(1–2):12–7.
[48] Hotz H, Kirsch B, Becker S, Müller R, Aurich JC. Combination of cold drawing and cryogenic turning for modifying surface morphology of metastable Austenitic AISI 347 steel. J Iron

Steel Res Int 2019;26(11):1188–98. https://doi.org/10.1007/s42243-019-00306-x.

[49] Talonen J, Hänninen H, Nenonen P, Pape G. Effect of strain rate on the strain-induced $\gamma \rightarrow \alpha$'-martensite transformation and mechanical properties of austenitic stainless steels. Metall Mater Trans A 2005;36:421–32. https://doi.org/10.1007/s11661-005-0313-y.

[50] Hotz H, Kirsch B, Becker S, von Harbou E, Müller R, Aurich JC. Improving the surface morphology of metastable austenitic steel AISI 347 in a two-step turning process. Procedia CIRP 2018;71:160–5. https://doi.org/10.1016/j.procir.2018.05.090.

[51] Noyan IC, Cohen JB. Residual stress. New York: Springer-Verlag; 1987.

[52] Brammertz PH. Die Entstehung der Oberflächenrauheit beim Feindrehen. Ind Anzeiger 1961;83(2):25–31.

[53] Becker S, Hotz H, Kirsch B, Aurich JC, von Harbou E, Müller R. A finite element approach to calculate temperatures arising during cryogenic turning of metastable Austenitic steel AISI 347. J Manuf Sci Eng 2018;140(6):101016. https://doi.org/10.1115/1.4040778.

[54] Hertz H. In: Jones, Schott, editors. On the contact of elastic solids. London: Macmillan; 1896.

[55] Kim JM, Chung HT. Electrochemical characteristics of orthorhombic LiMnO2 with different degrees of stacking faults. J Power Sources 2003;115(1):125–30. https://doi.org/10.1016/S0378-7753(02)00709-7.

[56] Schulze V. Characteristics of surface layers produced by shot peening. In: Wagner L, editor. Shot peening; 2006.

[57] Brinksmeier E, Cammett JT, König W, Leskovar P, Peters J, Tönshoff HK. Residual stresses — measurement and causes in machining processes. CIRP Ann - Manuf Technol 1982;31(2):491–510. https://doi.org/10.1016/S0007-8506(07)60172-3.